Inverse Lithography Source Optimization via Particle Swarm Optimization and Genetic Combined Algorithm

Haifeng Sun, Qingyan Zhang, Chuan Jin, Yanli Li, Yan Tang, Jian Wang, Song Hu, and Junbo Liu

***Abstract*—Inverse lithography technologies (ILTs) are critical for improving the imaging performance of lithography in advanced technology nodes. Pixel-based source optimization (SO), as an efficient part of ILTs, can be implemented *via* heuristic approaches to achieve high-performance lithographic imaging. In this paper, a SO approach based on a combination of the particle-swarm optimization and genetic algorithms (PSO–GA) is proposed to determine the optimal intensity distribution of the source *via* iterations. The pixelated source can be decoded into the optimized variables of the merit functions in the SO model. The proposed PSO–GA algorithm, as a high-efficiency hybrid algorithm, can transform the discrete SO problem into the optimal search solution for the merit function, thereby inversely enhancing the lithographic-imaging performance. In the forward-imaging model in the lithography, the extraction of the mask's effective diffraction spectrum is implemented to calculate the layout of resist patterns. The simulation results highlight the superior performance of the proposed approach in achieving pixelated SO over the traditional GA and PSO algorithm in terms of convergence capacity.**

***Index Terms*—Inverse lithography technologies, source optimization, particle-swarm optimization algorithm, genetic algorithm, hybrid algorithm.**

I. Introduction

Optical lithography is a key technology in the fabrication of very large-scale integrated circuits (VLSICs). With the critical dimension (CD) of the feature pattern in VLSICs continually shrinking toward the sizes of advanced technology nodes, image fidelity is becoming an increasingly important parameter in improving the performance of optical lithography [1], [2], [3], [4]. Inverse lithography technology (ILT), as a part of resolution-enhancement technologies, is essential to overcoming the optical proximity effect and promoting image fidelity [5], [6], [7]. As a significant ILT approach, pixelated source optimization (SO) has been proven to be necessary for improving the imaging performance of lithography in advanced technology nodes [8], [9]. Furthermore, it has been successfully applied by several institutions, such as ASML [10], [11], [12] and IBM [13], [14], to modulate the intensity distribution and incident angles of lithography-illumination sources in industrial applications [15], [16]. However, the highly complex representation of the source impacts the performance of the pixelated SO method. Furthermore, the high computation efficiency required to achieve further enhancements is a source of concern.

To enhance the performance of the pixelated SO methods, a set of algorithms have been proposed, including gradient-based [17], [18] and heuristic algorithms [19], [20]. In these methods, the pattern errors, as a generally utilized merit function in the iteration procedure, can be defined by calculating the cumulative sum of the difference between the resist pattern (RP) and the desired image with point-by-point. Moreover, multifarious merit functions have been employed to evaluate the simulation results and convergence effect in SO methods, such as the edge-placement errors, normalized-image log slope, and mask-error enhancement factor [19], [21], [22]. Thus, the threshold and the sigmoid functions can be employed to approximately represent the layout pattern after the resist effect is exerted on the wafer surface [23], [24]. Regarding the application of the gradient-based SO method, many studies have proven that the imaging performance of lithography can be improved by optimizing the source's intensity distribution [18], [25]. Peng et al. employed a gray-level pixel to represent the lithographic source and utilized the gradient-based SO method to improve the image fidelity and depth of focus [18]. Ding et al. employed the gradient-descent method to optimize the lithographic source and mask in the hybrid Hopkins–Abbe imaging model to enhance the optimization performance [25]. However, for a lithographic imaging process using a complicated resist model, it is not recommended to calculate the gradients of a highly complex merit function in the gradient-based SO model. Moreover, for the typical, local optimization methods, the convergence capability

Manuscript received 27 November 2022; accepted 29 November 2022. Date of publication 2 December 2022; date of current version 21 February 2023. This work is supported by the National Key Research and Development Plan under Grant 2021YFB3200204, in part by the National Natural Science Foundation of China (NSFC) under Grants 61604154, 61875201, 61975211, and 62005287, in part by the Youth Innovation Promotion Association of the Chinese Academy of Sciences under Grant 2021380, and in part by the Project of the Western Light of Chinese Academy of Science. *(Corresponding author: Junbo Liu.)*

Haifeng Sun is with the Institute of Optics and Electronics, Chinese Academy of Science, Chengdu 610209, China, also with the School of Automation Engineering, University of Electronic Science and Technology of China, Chengdu 611731, China, and also with the University of Chinese Academy of Sciences, Beijing 100049, China (e-mail: hf_sun0804@163.com).

Qingyan Zhang, Yanli Li, and Song Hu are with the Institute of Optics and Electronics, Chinese Academy of Science, Chengdu 610209, China (e-mail: thomas.zhang991122@gmail.com; liyanli@ioe.ac.cn; husong@ioe.ac.cn).

Chuan Jin, Yan Tang, Jian Wang, and Junbo Liu are with the Institute of Optics and Electronics, Chinese Academy of Science, Chengdu 610209, China, and also with the University of Chinese Academy of Sciences, Beijing 100049, China (e-mail: 843034626@qq.com; ty0513@163.com; wangjian@ioe.ac.cn; ljbopt@126.com).

Digital Object Identifier 10.1109/JPHOT.2022.3226266

This work is licensed under a Creative Commons Attribution 4.0 License. For more information, see https://creativecommons.org/licenses/by/4.0/

of gradient-based approaches is restricted by the high-dimension variate matrices of the pixelated source.

Heuristic algorithms, such as the genetic algorithm (GA) [26], [27], particle-swarm optimization (PSO) [28], [29], and differential evolution [30], are commonly applied to handle optimization challenges because they are free of complex optimization structures and tedious gradient calculations that search for the global suboptimal solution to the merit function. Moreover, it is convenient to simplify the complex challenges; for instance, the optimization of the lithographic source can be simplified to the calculation of the optimal value of the merit function [31]. Additionally, these approaches have been widely employed to improve the performance of lithographic imaging simulations. Tian et al. simulated the global optimization of the lithographic source over multiple patterns to emphasize the predominant convergence capability of SO methods based on heuristic algorithms [32]. Yang et al. proposed a multipole source representation to denote the low pupil-filling-ratio freeform, which was combined with a GA to significantly enhance the global SO performance [33]. Fuhner et al. utilized a GA to optimize mask and illumination geometries, and the simulation results demonstrated the successful application and future potential of the proposed approach [34]. Chen et al. utilized the covariance matrix adaptation evolution strategy with a new source-representation method to inversely optimize the lithographic source and mask, satisfying the high optimization-capacity and convergence-efficiency requirements in lithographic-imaging simulations [31]. Wang et al. employed PSO to evaluate the intensity distribution of the source, in which pattern fidelity was adopted as the fitness function to evaluate the simulation results [20]. In research works, heuristic algorithms have been proven to exhibit considerable potential for improving the performance of lithographic imaging [30], [35], [36], [37]. Nevertheless, the existing heuristic algorithms that are generally applied in optimization models make it difficult to deviate from the local optimum in the case of a complex merit function [38], [39].

To improve the search capability of these standard global methods at the optimization stage, it is more efficient for their hybrid form. [40], [41], [42], [43]. Particularly, the hybrid PSO algorithm has been generally applied to solve the optimization problem of complex models. Cao et al. embedded the local search method into PSO to significantly enhance the global search capability of this method [42]. Tian et al. utilized the hybrid PSO based on the multi-objective differential-Evolution approach to optimize the real-word emergency scheduling problem of the forest fire [43]. Therefore, for a complex model, it is essential to employ a hybrid algorithm to search the optimum solution.

In this paper, a highly efficient hybrid algorithm combining particle-swarm optimization with genetic algorithm (PSO–GA), is proposed to inversely optimize the intensity distribution of the pixelated source in lithographic-imaging simulations. Although the PSO model shows promise in the global search for the complicated lithographic inverse optimization model, the convergence to global optimality is not accomplished directly. To solve this challenge, crossover and mutation operations involving GA are employed to modify the particle variables in PSO. In these simulations, two merit functions are utilized to evaluate the convergence results: the pattern errors (PEs) and the edge placement errors (EPEs). Moreover, we employ a typical lithographic-imaging model based on the effective spectrum extraction of the mask to improve the imaging performance. The simulation results confirm that SO approach based on PSO–GA exhibits better convergence performance than the standard GA and PSO algorithm.

The organization of this paper is as follows. The forward lithographic imaging model is described in Section II-A. The proposed PSO–GA approach utilized to achieve SO is introduced in Section II-B. Section III provides the simulation results and discussions, followed by the summary in Section V

II. Methodology

A. Forward Lithographic Imaging Model

In this section, the imaging process of the lithography system is explained using mathematical formulas. For a typical lithography simulation, the lithographic imaging model is composed of two indispensable units: the illumination source and the projection objective. The former can produce incident light in the form of Kohler illumination. The rays are transmitted through the mask to generate the diffraction light with the feature pattern information. The latter collects the diffraction information of the feature patterns. However, due to the optical diffraction limitation of lithography, the projection objective, which can be regarded as a low-pass filter, can limit the participation of higher-order diffraction during the formation of the desired aerial image in the traditional illumination methods. This phenomenon results in a loss of the lithographic-imaging fidelity. Therefore, it is essential to improve the imaging performance of lithography *via* SO. Furthermore, the intensity distribution of the aerial image can be calculated *via* the Abbe theory, as follows [44], [45]:

$$I\left(x_i, y_i\right) = \iint_{-\infty}^{+\infty} S(f,g) \left[\left|\iint_{-\infty}^{+\infty} P(f+f', g+g') M(f',g')\, e^{-i2\pi[x_i f' + y_i g']} df' dg'\right|^2\right] df\, dg \tag{1}$$

Here, I represents the intensity distribution of the aerial image; (x_i, y_i) denotes the spatial coordinates on the image plane; (f, g) and (f', g') represent the normalized-frequency-domain coordinates of the pupil and the mask, respectively; S is the lithographic illumination source shape; P is the optical-transfer function of the projection objective; M is the frequency spectrum of the mask pattern, which can be obtained *via* 2D fast Fourier transform (FFT).

The forward lithographic imaging model, as a typical partially coherent imaging (PCI) model, can be dissected into a set of coherent imaging processes. All the spectrums can be established under the same spectral coordinate system using the mask's frequency spectrum as the standard. Assuming that the quadrate mask's length is $2L$, the coordinate range can be set to $[-L, L]$. Therefore, the coordinate range of the frequency spectrum is $[-N/2L, N/2L]$, where the sampling point number, N, denotes

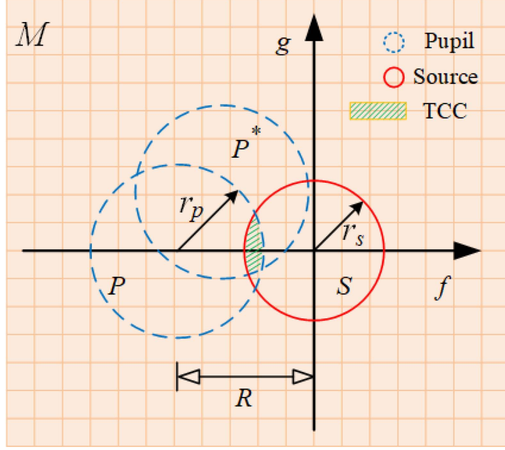

Fig. 1. Position relationship between the source and the pupil in the frequency spectrum of the mask. The blue and red circles represent the pupil and source, respectively, the green shaded part represents the transmission cross-coefficient (TCC) matrix; r_s represents the source radius; r_p is the pupil's radius representing the cut-off frequency; P and P^* are the pupil matrix and the pupil conjugate matrix, respectively; R is the extreme shifting length of the pupil matrices' center relative to the source's center.

the number of pixels for the lateral dimension. According to the theory of lithographic imaging, the cut-off frequency of the pupil is NA/λ, where NA and λ are the numerical aperture and illumination wavelength, respectively. The partial coherent factor (σ) of the illumination source can be defined as the ratio of the source radius to the pupil radius, $\sigma = r_s/r_p, 0 < \sigma < 1$. Therefore, the radii of the source and pupil matrices can be respectively represented by $r_s = \sigma NA/\lambda$ and $r_p = NA/\lambda$.

Fig. 1 illustrates the change in the pupil's position relative to the source on the frequency spectrum of the mask. In the Hopkins imaging model [44], [46], the position of the pupil is shifted relative to the valid pixel position of the source to generate the aerial image in the imaging simulation (the pupil and source are respectively represented by the blue and red circles in Fig. 1). The transmission cross-coefficient (TCC) matrix is represented by the green shaded area formed by the overlap of the three circles: the source matrix, pupil matrix, and pupil-conjugate matrix. Along the f axis, the maximum movement length of the pupil matrix can be assumed to be R, $0 \le R < r_s + r_p$. Therefore, the movement region of P is the circle with radius R.

The diffraction spectrum, which is utilized to generate the lithographic aerial image, is only a part of the complete spectrum. Fig. 2 illustrates the process of extracting the valid diffraction spectrum. The complete diffraction spectrum can be obtained by applying 2D FFF to the mask. Thus, the valid diffraction spectrum matrix can be acquired using the following rule:

$$M_{ext} = M(f,g), \sqrt{f^2+g^2} \le R_f, \tag{2}$$

where M_{ext} represents the valid diffraction spectrum matrix of the mask. The region of the valid diffraction spectrum is represented by the circle with radius R_f. Assuming that the radius of the pixelated source matrix is smaller than that of the pupil matrix, then

$$0 \le R_f \le r_s + 2r_p \Rightarrow 0 \le R_f \le 3NA/\lambda. \tag{3}$$

In a partially coherent system, the PCI process can be expressed as the sum of the aerial images produced by a series of coherent imaging processes. Additionally, the coherent imaging process can be represented as a spectral integral, as follows:

$$C(\hat{x}_i,\hat{y}_i;f,g) = \left| \iint_{-\infty}^{+\infty} P(f+f',g+g') \times M(f',g')\, e^{-i2\pi[\hat{x}_i f' + \hat{y}_i, g']} df'dg' \right|^2 \tag{4}$$

$$C_{ext}(\hat{x}_i,\hat{y}_i;j,k) = \left| \sum_{j=1}^{N_{ext}} \sum_{k=1}^{N_{ext}} P(j+j',k+k')\, M(j',k') \times e^{-i2\pi[f'(j,k)x(\hat{x}_i,\hat{y}_i) + g'(j,k)y(\hat{x}_i,\hat{y}_i)]} \right|^2 \tag{5}$$

Here, C_{ext} represents the extracted illumination cross coefficient (ICC), and (4) confirms the generation of a coherent image by a unit source point in the pixelated source. The discrete coherent imaging process can be explained by (5), where $\hat{x}_i, \hat{y}_i, j, k = 1, 2, 3, \ldots, N_{ext}$. Further, N_{ext} denotes the sampling number of the extracted valid diffraction spectral in the lateral dimension. Therefore, for the discrete extended illumination source in lithography, the lithographic aerial image can be expressed as follows:

$$I_{ext}(\hat{x}_i,\hat{y}_i) = \sum_{m=1}^{N_s} \sum_{n=1}^{N_s} S(m,n) C_{ext}(\hat{x}_i,\hat{y}_i;m,n), \quad m,n = 1,2,3,\ldots,N_s \tag{6}$$

In (6), N_s represents the sampling number of the pixelated source in the lateral dimension. To guarantee the same dimension between the results of (1) and (6), the interpolation operation must be implemented. Resultantly, (6) can also be expressed as (7) *via* the multiplication of low-dimensional matrices:

$$\boldsymbol{I}_{ext} = \boldsymbol{C}_{ext} \times \boldsymbol{S}_{ext}, \tag{7}$$

where $\boldsymbol{S}_{ext}$ is the 1D matrix that consists of the effective source points employed to generate the aerial image. Let $\boldsymbol{I}_{ext}$, $\boldsymbol{C}_{ext}$, and $\boldsymbol{S}_{ext}$ be represented by the real matrices, denoted by $\boldsymbol{I}_{ext} \in \mathbb{R}^{N_{ext}^2 \times 1}$, $\boldsymbol{C}_{ext} \in \mathbb{R}^{N_{ext}^2 \times N_{s,ext}^2}$, and $\boldsymbol{S}_{ext} \in \mathbb{R}^{N_{s,ext}^2 \times 1}$, respectively. Fig. 3 demonstrates the process of manipulating the matrices in (7).

Assuming that the illumination source is annular, as shown in Fig. 3(e), the number of valid source points becomes $N_{s,ext}$. To expediently implement the matrix operation, the 2D source matrix, S, can be transformed into the 1D matrix, $\boldsymbol{S}_{ext}$, by respectively carrying out $Extr[\centerdot]$ and $Reshape[\centerdot]$. In $\boldsymbol{ICC}_{ext}$, each column represents the 1D ICC matrix, which can be generated by converting the 2D C_{ext} of (5) into the 1D vector matrix. According to (7), the multiplication operation of $\boldsymbol{C}_{ext}$ and $\boldsymbol{S}_{ext}$ can generate the 1D $\boldsymbol{I}_{ext}$ matrix. With the reconstruction

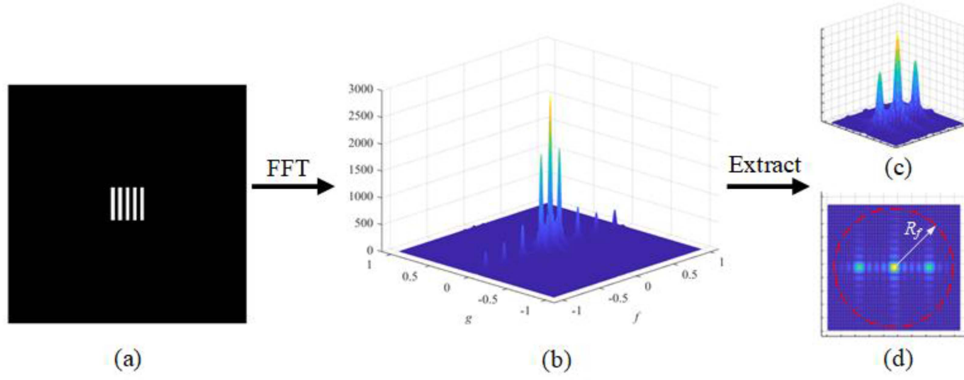

Fig. 2. Schematic diagram of the extraction process of the valid diffraction spectrum. (a) Mask layout; (b) Complete diffraction spectrum of the mask; (c) 3D extracted valid diffraction information; (d) 2D extracted valid diffraction information. In (d), the red dotted circle represents the valid spectrum range, where the radius of this circle is R_f. FFT denotes the 2D fast Fourier transform operation.

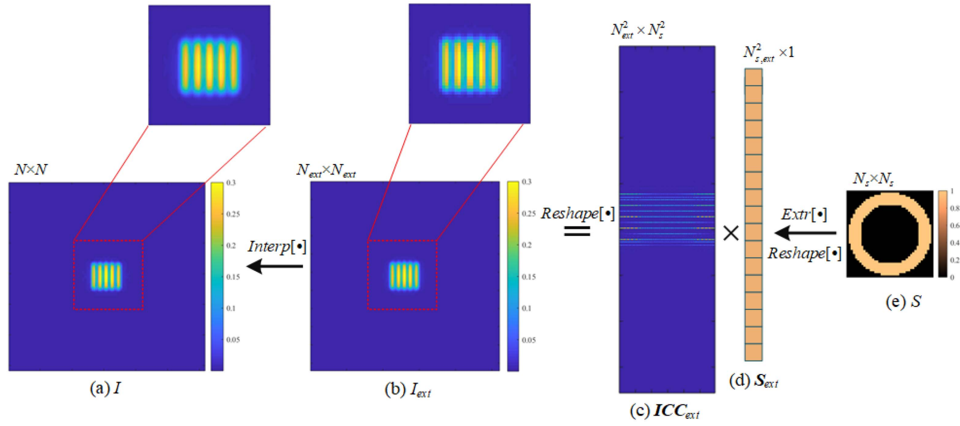

Fig. 3. Illustration of the generation of the lithographic aerial image based on (7). (a) $N \times N$ aerial image; (b) $N_{ext} \times N_{ext}$ aerial image; (c) Extracted illumination cross-coefficient matrices; (d) Extracted valid source matrices; (e) Annular illumination source. $Interp[\cdot]$ can transform I_{ext} into Iusing the interpolation method. $Reshape[\cdot]$ is the function for reconstructing the matrix, which can execute the mutual conversion between the 1D and 2D vector matrices. $Extr[\cdot]$ can extract the valid source point to accomplish the PCI process from S.

executed by $Reshape[\cdot]$, the 2D extracted aerial image of I_{ext} can be achieved from the 1D vector matrix of $\boldsymbol{I}_{ext}$, where there is a difference in the matrix dimension between I_{ext} and I. To calculate the RP on the wafer, it is critical to ensure that the output aerial image has the same matrix size as that of the input mask. Upon executing the interpolation operation using $Interp[\cdot]$, $I \in \mathbb{R}^{N\times N}$ can be generated from I_{ext}, as shown in Fig. 3(b)–(a).

To achieve the optimal intensity distribution of the lithographic source in the SO model, the layout of RP can be generated using the resist effect, which is approximated using the sigmoid function. Therefore, the layout of RP obtained by the resist effect can be expressed as follows:

$$I_{RP} \approx \Gamma\{I(x_i, y_i)\} = \frac{1}{1 + \exp[-\alpha(I(x_i, y_i) - t_r)]}. \quad (8)$$

Here, I_{RP} represents the layout of RP. The function, $\Gamma\{\cdot\}$, is a regular S-type function, which approximately replaces the threshold value; α is the steepness index, and t_r is the threshold value of the photoresist.

B. Flow of the PSO–GA Approach

The flow of the PSO–GA approach is derived in this section. In this paper, the proposed hybrid PSO–GA, as a heuristic algorithm, only requires the merit function with the original format that has the free-gradient operation. To visibly estimate the optimization results in the SO process, the PEs and EPEs are utilized as the merit functions. The PE formula representations are as follows:

$$\Pi\{\boldsymbol{x}_s\} = \underset{x_i, y_i}{\text{minimize}} \sum\sum |I_{RP}\{\boldsymbol{x}_s\}(x_i, y_i) - M^*(x_i, y_i)|, x_i, y_i \in \mathbb{Z}^N \quad (9)$$

The function, $\Pi\{\boldsymbol{x}_s\}$, in (9), which can help achieve a value close to the global minimum in the iteration procedure, is incorporated in the accumulation of the absolute value of the difference between the output RP and the input mask pattern, M^*. Further, $\boldsymbol{x}_s$ represents the variable matrix of the extracted valid source points, which can be updated in each loop, and $\boldsymbol{x}_s \in [0, 1]$. For the EPEs, the monitored regions of M^* marked

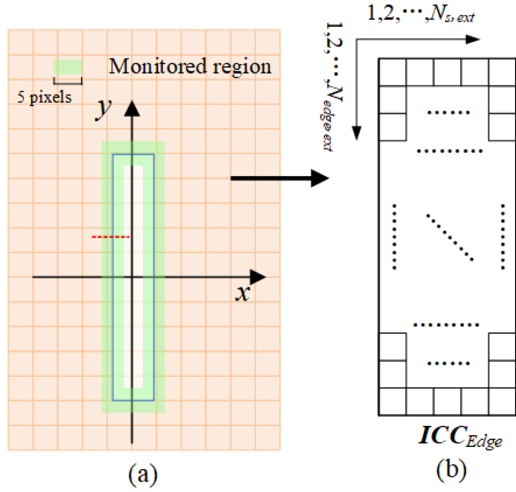

Fig. 4. Formation of ***ICC*** in the marked region. (a) Position of the marked region; (b) ***ICC*** matrix of the monitored region. The edge range of the feature pattern is marked in the green region, and there are 5-pixel points on the red dotted line of this region. The $\boldsymbol{ICC}_{Edge}$ matrix can be formed by reconstructing the extracted marked regions, which is denoted by the point where its size is $\boldsymbol{ICC}_{Edge} \in \mathbb{R}^{N_{edge,ext} \times N_{s,ext}}$.

in the assigned length range are illustrated in Fig. 4, which are 2-pixel points inside and outside the margins of M^*.

In Fig. 4(a), the green region represents the monitored pixels, which are utilized to calculate the change in the EPEs. The matrix, $\boldsymbol{ICC}_{Edge}$, shown in Fig. 4(b), can be generated by reconstructing the extracted pixel points in the green region into the 1D vector matrix. Thus, according to the different positions of the valid source points, the 1D vector matrix can be arranged into the $N_{edge,ext} \times N_{s,ext}$ matrix. Therefore, the EPEs can be formulated as

$$\Pi^* \{\boldsymbol{x}_s\} = \underset{x'_i}{\text{minimize}} \sum |\boldsymbol{ICC}_{Edge} \boldsymbol{S}_{ext} \{\boldsymbol{x}_s\} (x'_i) - M'_{ext} (x'_i)|, x'_i \in \mathbb{Z}^{N_{edge}} \quad (10)$$

In (10), the matrix, M'_{ext}, can be formed by extracting these points with the marked position in Fig. 4. The size of M'_{ext} is the same as the result of $\boldsymbol{ICC}_{Edge} \boldsymbol{S}_{ext}\{\boldsymbol{x}_s\}$, and they are both $N_{edge} \times 1$ matrices, where N_{edge} represents the number of extracted points from the green region.

To ensure high-performance lithographic imaging, high-efficiency optimization approaches as a part of ILTs are indispensable. Thus, a hybrid PSO–GA approach is proposed to improve the lithographic-imaging performance in the PCI process. Although PSO exhibits the good convergence performance in the early stage of the iteration process, the relatively low convergence aptitude causes the value of the merit function to fall to the local optimum. To enhance the optimization performance of the PSO algorithm, the mutation operation and crossover operation of GA are embedded into the PSO procedure. This approach has been used in the previous studies. Piotr et al. proposed to utilize the neuro-fuzzy system to improve the performance of a hybrid method combining PSO with GA [40]. Shang et al. applied the

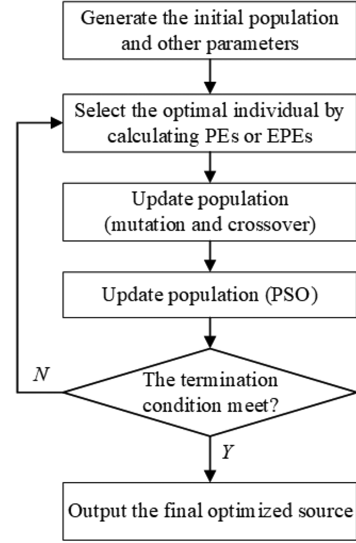

Fig. 5. Flowchart of the proposed PSO-GA approach.

combination of GA and PSO into the management of workshop production scheduling to improve the production efficiency and product quality [47]. For the constrained engineering optimization problems, Zhu et al. used a dynamic adaptive inertia factor to balance the convergence rate and global search capacity of PSO, and employed the operators of GA, such as a selection operator, crossover operator, and n-point random mutation operator, to enhance the convergence ability [48]. Based on the random search mechanism, GA is capable of global optimization, and its solution is considered robust [49], [50]. Moreover, the superior scalability of GA enables it to be easily combined with other algorithms.

In the proposed PSO–GA approach, the mutation and crossover operations are utilized to update the initial variates of the pixelated source. Subsequently, these updated variates are employed as the inputs for the PSO to accomplish the entire iteration process. The optimization flow of the proposed approach is shown in Fig. 5. Assuming that the initial variate matrix named as the population is $\boldsymbol{P}$, and $\boldsymbol{P}$ is represented by a real $N_p \times N_{s,q}$ matrix denoted by $\boldsymbol{P} \in \mathbb{R}^{N_p \times N_{s,q}}$, where N_p and $N_{s,q}$ respectively represent the individual number and the variate number of the valid source points in the first quadrant, the complete source can be achieved by executing the mirror operation according to the optical symmetry of the lithographic source. In the GA process, the following formulas can decide the result of the mutation operation:

$$\Delta\varepsilon = \eta_1 * (1 - t/\tau)^2 \quad (11)$$

$$\begin{cases} \boldsymbol{P}(k,m) = \boldsymbol{P}(k,m) * (1 - \Delta\varepsilon), & 0 < \eta_1 < \varsigma'_{mum}, \; \varsigma'_{mum} \in (0,1); \\ \boldsymbol{P}(k,m) = \boldsymbol{P}(k,m) * (1 + \Delta\varepsilon), & \text{otherwise.} \end{cases} \quad (12)$$

Here, the increment, $\Delta\varepsilon$, can be randomly updated with an increasing number of iterations, where η_1, t, and τ represent the random number, current iteration number, and total iterations,

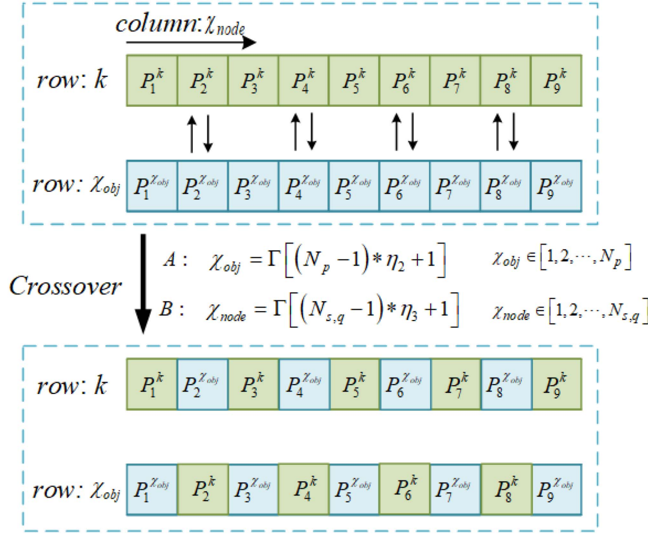

Fig. 6. The crossover operation. Formulas *A* and *B* respectively represent the indexed row and column in population ***P***. $\Gamma[\cdot]$ is the rounding operation function. N_p and $N_{s,q}$ respectively represent the number of individuals in population ***P*** and the number of variates in every individual. Both η_2 and η_3 are generated by the random function, $\eta_2, \eta_3 \in (0, 1)$.

respectively. In (12), the variates of the individuals in ***P*** can be indexed by the position (k, m), and the values of η_1 and ς'_{mum} determine the variable tendency of these variates in each iteration.

To maintain the diversity in population ***P***, the crossover operation of GA is necessary to improve the search performance of the proposed approach. The multipoint crossover strategy is employed to improve the randomness of the variate-update process and expand the search scope. The selected part of this crossover operation in every individual can be determined by the index position $(\chi_{obj}, \chi_{node})$, which is illustrated in Fig. 6. Assuming that the individual in the k_{th} row needs to be updated in the current loop for the crossover process, row χ_{obj} of the individual can be utilized as the target to perform the crossover operation. In addition, these variates indexed by column χ_{node} in row χ_{obj} of the individual are selected to swap with row k_{th}.

Thus, population ***P***, generated by the mutation and crossover operations of GA, is inputted into the PSO model. A nonlinear adaptive control strategy is employed to improve the search performance of PSO in the optimization process. The probability of maintaining the local optimum can be reduced using this strategy. Meanwhile, the search scope can be expanded by updating the weight coefficient. This strategy can be expressed by the following formula:

$$w(t) = \frac{w_{\max} + w_{\min}}{2} + \Psi\left[-\zeta + \frac{2\zeta(\tau - t)}{\tau}\right]\frac{w_{\max} - w_{\min}}{2}, \tag{13}$$

where $w(t)$ represents the weight coefficient in the t_{th} iteration, which is utilized as the coefficient of calculating the velocity of searching variates in population ***P***; $w_{\max}$ and $w_{\min}$ represent the maximum and minimum weight coefficients, respectively; $\Psi[\cdot]$ is the hyperbolic tangent function, which is used to control the gradient process of the weight coefficient according to the value of the constant, ζ. Therefore, the variation denoted as the particle-search velocity in every individual can be represented as

$$\upsilon_k(t+1) = w\upsilon_k(t) + c_1\eta_4\left[Q_{best,k}(t) - P_k(t)\right] + c_2\eta_5\left(G_{best} - P_k(t)\right) \tag{14}$$

$$P_k(t+1) = P_k(t) + \upsilon_k(t+1) \tag{15}$$

Algorithm 1: Flow of the PSO–GA Algorithm in the SO Simulation.

Input
Size of population ***P***: N_P;
Number of variates in an individual: $N_{s,q}$;
Mutation and crossover factors: ς_{mum}, ς_{cro};
Learning factors: c_1, c_2;
Maximum and minimum search velocities: $\upsilon_{\max}$, $\upsilon_{\min}$;
Maximum and minimum weight coefficients: $w_{\max}$, $w_{\min}$;
Maximum number of iterations: τ.

Step 1
Generate the initial search velocity matrix υ) and the source population (***P***) using the random function.
Calculate *I*, *PEs*, and *EPEs* using (7), (9), and (10), respectively.
Select the optimal source individual according to the lowest *PEs* and *EPEs*.

Step 2
While $t \leq \tau$ Do, execute the mutation operation,
For $i = 1$ to N_P
If $\eta_{mum} < \varsigma_{mum}$, $\eta_{mum} = rand$, then
Execute (11)–(12);
End If;
If ***P***(*i*) is not feasible, then
$\boldsymbol{P}(i) = rand$;
End If;
End For;
For $i = 1$ to N_P
If $\varsigma'_{cro} < \varsigma_{cro}$, $\varsigma'_{cro} = rand$, then
Calculate the index position of the source variates in each individual using Formulas A and B in Fig. 5;
End If;
End For;
For $i = 1$ to N_P
Calculate *w* using (13);
Update υ using (14);
If $\boldsymbol{\upsilon}(i)$ is not feasible, then
$\boldsymbol{\upsilon}(i) = rand$;
End If;
Update the source individual, $P(i)$, using (15);
If $P(i)$ is not feasible, then
$P(i) = rand$;
End If;
Respectively calculate *I*, *PEs*, and *EPEs* using (7), (9), and (10) according to ***P***;
Select the current best source individual *P*, *PEs*, and *EPEs*;
Update the best *P*, *PEs,* and *EPEs* according to the index;
End While.

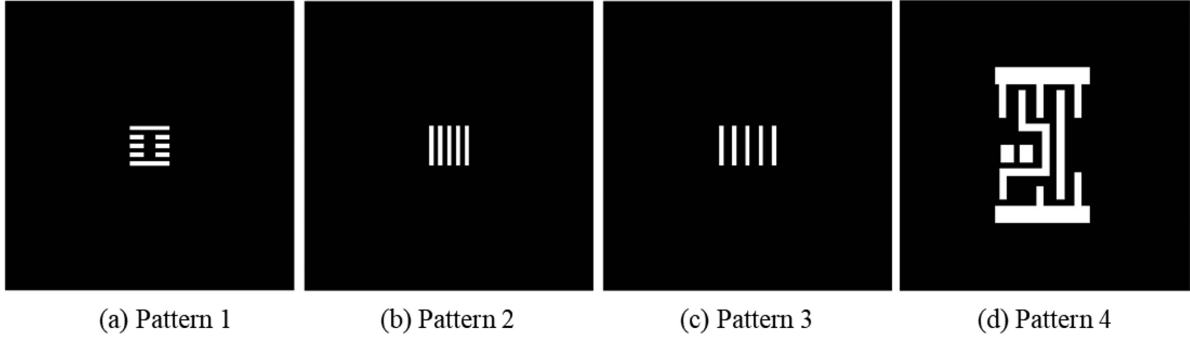

Fig. 7. The three mask patterns utilized in the simulations. (a) Horizontal block pattern; (b) and (c) are both vertical array patterns with duty ratios of 1:1and 1:2, respectively; (d) Logic circuit pattern.

In (14), $\upsilon_k(t)$ represents the variation of the k_{th} individual, P_k, in the t_{th} iteration, where c_1, c_2 represent the learning factor, and η_4, η_5 are the random numbers. The current best value, $Q_{best,k}$, and global best value, G_{best}, can be calculated with the merit function in the lithographic-imaging process. Therefore, in the loop for updating population $\boldsymbol{P}$, the current individual can be calculated using (15). The flow of the proposed PSO–GA algorithm in this work is illustrated in Algorithm 1.

III. Simulations

In this section, a set of simulation results is provided to verify the superior optimization performance of the proposed method to improve the performance of the lithographic-imaging process. The pixelated SO model is based on the 193 nm immersion lithography system in the 45-nm technology node. The numerical aperture (*NA*) of the imaging system is 1.35. The effective spectrum-extraction approach is utilized to achieve the PCI step of the lithography. In these simulations, the annular source shape is used as the initial illumination source. The inner partial coherent factor (σ_{inner}) and outer partial coherent factor (σ_{outer}) are 0.68 and 0.95, respectively. The pixelated source pattern in this model is a $N_s \times N_s$ matrix, where $N_s = 41$. To reduce the degree of discretization in the intensity distribution and achieve a continuous gray gradient, the source is blurred *via* gaussian filtering. The sigmoid function is employed to approximately simulate the process of forming the RP, where $\alpha = 85$ and $t_r = 0.21$.

To evaluate the performance of the proposed method, four mask patterns are employed to accomplish the SO simulations (Patterns 1–4), as shown in Fig. 7. The first pattern is the horizontal block pattern, the middle two are both vertical array patterns with duty ratios of 1:1 and 1:2, and the last is a typical logical-circuit pattern. They are all $N \times N$ matrices, where $N = 521$. In this SO model, the size of a single pixel is 5.625 nm × 5.625 nm. For convenience in executing the SO procedure, only valid pixels in this source are extracted to form a $N_{s,ext} \times 1$ matrix, where $N_{s,ext} = 576$. As a typical 4-fold symmetry structure, 144 pixels are utilized as the optimized variates in the iterative process. Using the mirror operation, the complete source shape can be directly recovered. Furthermore, two merit functions are employed as the iteration objectives to achieve the optimum source shape: PEs and EPEs. Three algorithms, including GA, PSO, and the proposed algorithm, are utilized to execute the SO simulations with different merit functions and mask patterns. For a reasonable comparison of the simulation results, the valid pixel values of the initial source, which are generated by the random function, were kept constant for the same mask pattern

Fig. 8 illustrates the SO simulation results using different optimization algorithms with different mask patterns and the PE merit function as the optimization objective. The three rows from top to bottom show the optimization results of the source and the resist patterns obtained using three different optimization algorithms: GA, PSO, and PSO–GA. Based on the type of mask pattern, the simulation results can be divided into three columns. From left to right, they are Patterns 1–3, respectively. Further, each column exhibits the intensity distribution of the optimized source and resist patterns. In the optimization results of the second row, the grayscale changes among all the optimized sources are inconspicuous in the intensity distribution, as shown in Fig. 8(g), (i), and (k). On the contrary, the grayscale gradients show outstanding performance for the optimized source in the first and third rows. This is because the excellent performance of the PSO algorithm enables the easy achievement of the local optimum for the complex PCI model. The intensity distributions of the sources optimized by GA and the proposed method both show similar tendencies. In the SO model based on GA, the source shape with Pattern 1 is composed of four arcs, which are shown in Fig. 8(a). The vertical dipole illumination and four arcs in the inclined top, shown in Fig. 8(c), constitute the final source shape for Pattern 2. Additionally, the source shape for Pattern 3 has the approximate quadrupole illumination mode, where the patterns represented in Fig. 8(e) in four directions are closer to the circles. However, for the proposed SO method, the results of the optimizing sources, as shown in Fig. 8(m) and (q), show more pronounced changes corresponding to Patterns 1 and 2, respectively. In the layout of the resist patterns, there are no discernible differences. For the PEs with different algorithms, the proposed SO method can achieve large declines. Table I lists the PEs at the end of the iteration process.

Meanwhile, the optimization results for the simulations with different SO methods executed using the EPE merit function are shown in Fig. 9, including the optimized sources and the resist

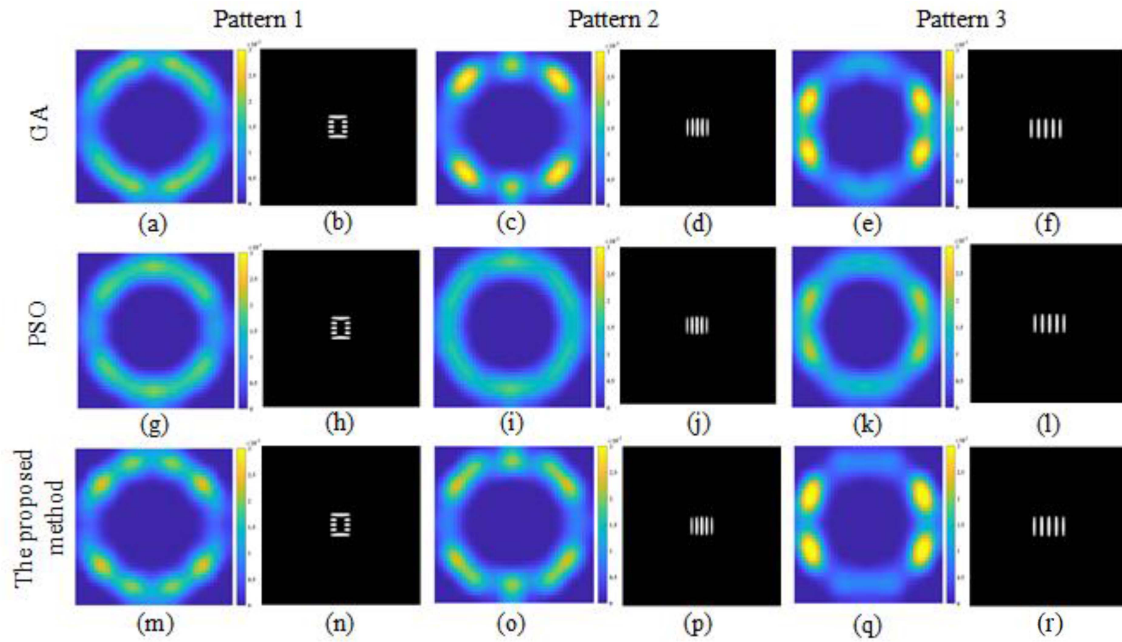

Fig. 8. Simulation results using the merit function PEs for the simple patterns. From top to bottom: Simulation results using GA, PSO, and PSO–GA. From left to right: The optimized source and resist pattern corresponding to the three patterns: Pattern 1, Pattern 2, and Pattern 3, respectively. Columns 1, 3, and 5: The intensity distribution of optimized source. Columns 2, 4, and 6: The resist patterns generated using the optimized source.

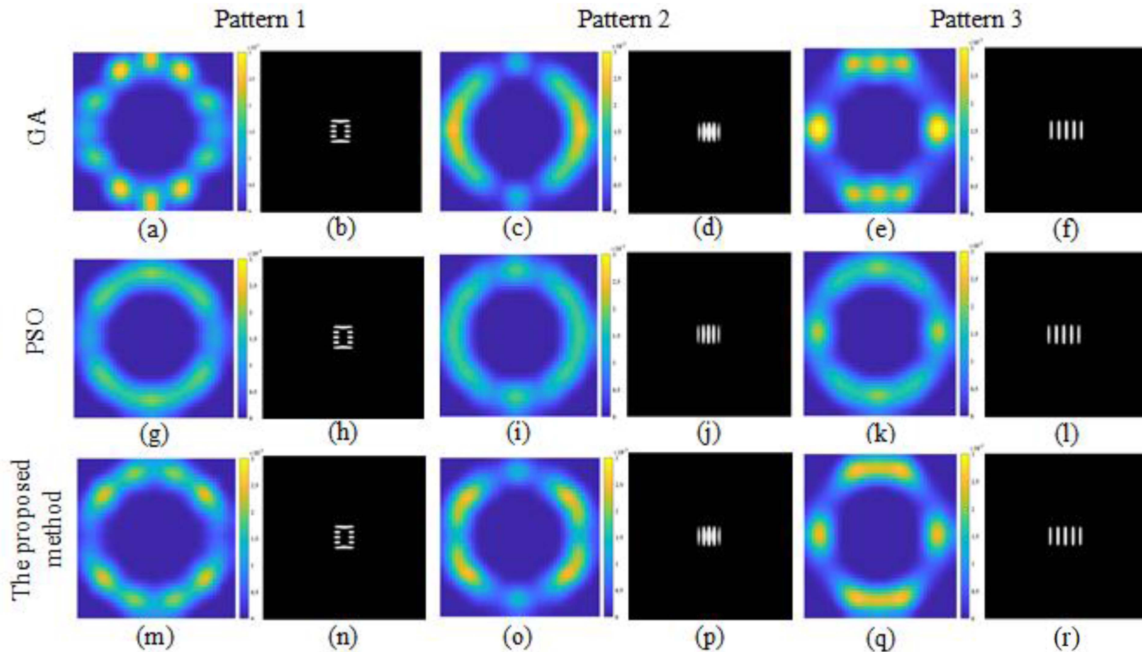

Fig. 9. Simulation results via the merit function EPEs for the simple patterns. From top to bottom: Source shape and resist patterns optimized via GA, PSO, and PSO–GA. From left to right: Three sets of simulation results based on different patterns in two columns, which are Pattern 1, Pattern 2, and Pattern 3, respectively.

patterns. These illustrations are arranged in the same manner as in Fig. 8. Similarly, it is evident that PSO still keeps the local optimum in the SO model, which is consistent with the results obtained with the PEs. The intensity distribution of the optimized sources for GA is evidently different from that in Fig. 8. However, for Patterns 1 and 2, there are similar intensity distributions between Figs. 8 and 9. Although there is a difference in intensity, the source shape in Fig. 8(q) is similar to that in Fig. 9(q). Comparing the optimization performance of the RPs based on the merit functions, PEs and EPEs, it is evident that there are two similar sets of results that are achieved using Patterns 1 and 3, respectively. However, the optimization results using Pattern 2 have a more noticeable difference. The EPEs simulated by different optimization algorithms are listed in Table II.

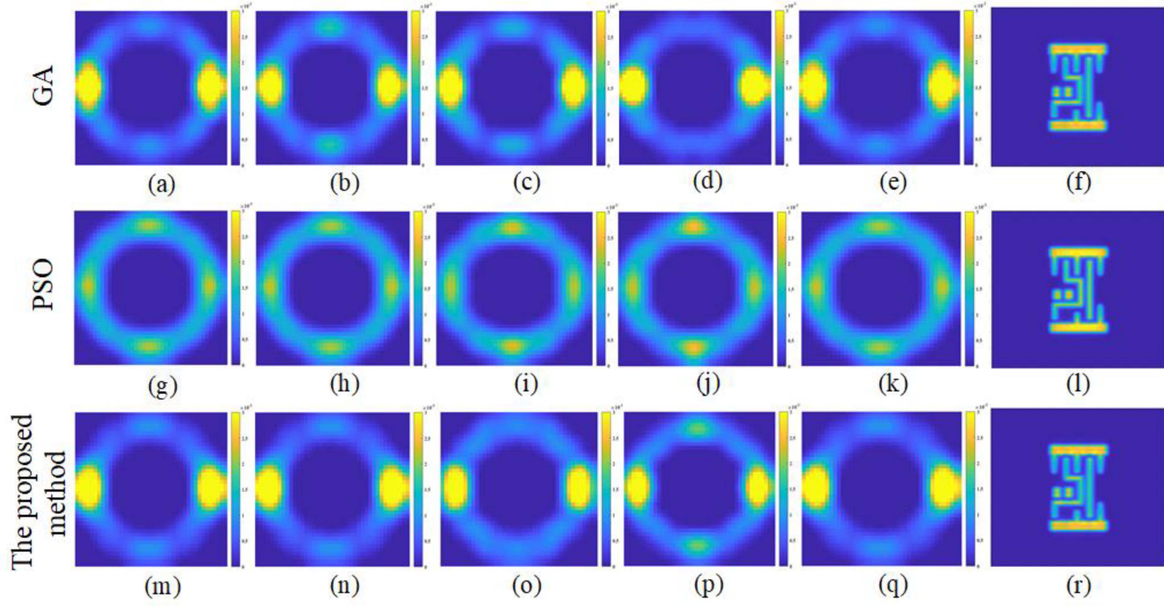

Fig. 10. Simulation results *via* the PE merit function for the logical-circuit pattern. From top to bottom: Simulation results obtained using GA, PSO, and PSO–GA. The optimized sources are shown in columns 1–5. The last column shows the intensity distribution of the aerial image.

TABLE I
COMPARISON OF THE OPTIMAL PEs WITH DIFFERENT OPTIMIZATION ALGORITHMS

	Pattern 1	**Pattern 2**	**Pattern 3**
GA	1558.67	1928.04	1092.71
PSO	1570.21	1957.27	1133.91
PSO–GA	1539.99	1903.98	1048.79

TABLE II
COMPARISON OF THE OPTIMAL EPEs WITH DIFFERENT OPTIMIZATION ALGORITHMS

	Pattern 1	**Pattern 2**	**Pattern 3**
GA	160.95	154.61	193.04
PSO	214.67	251.78	338.37
PSO–GA	136.01	120.49	163.92

To ensure the feasibility of the proposed method in practical applications, a typical logical-circuit pattern was employed to complete the SO simulations. The optimized sources and the intensity distribution of the aerial image *via* the PE merit function are shown in Fig. 10. The simulations using different optimization algorithms were all performed five times. From top to bottom, the displayed simulation results were achieved using GA, PSO, and PSO–GA, chronologically. The first five columns are the optimized source, and the last column shows the intensity distribution of the aerial image. The distribution rules of the simulation results *via* the EPE merit function in Fig. 11 are consistent with those described above. Comparing the simulation results obtained with the two merit functions, the optimized sources obtained by the PSO algorithm have indistinct intensity distributions. Nevertheless, the SO results obtained using GA and PSO–GA are outstanding. In the simulation

TABLE III
AVERAGE EXECUTION TIME (S) OF THESE SIMULATIONS UNDER DIFFERENT CONDITION

		Pattern 1	Pattern 2	Pattern 3	Pattern 4
PEs	GA	2032.54	1846.53	1795.64	2464.57
	PSO	1475.694	1198.47	1257.81	2163.67
	PSO-GA	1840.262	1615.83	1463.58	1958.28
EPEs	GA	1365.87	1012.48	985.71	1584.17
	PSO	956.42	879.48	906.78	1085.29
	PSO-GA	1058.51	986.78	1018.62	1219.76

results *via* the different merit functions, the SO results using the PSO–GA algorithm are approximate to the results obtained using the GA algorithm. Furthermore, the intensity distribution of the source with the PE merit function takes the form of horizontal bipolar illumination. The optimized-source shapes, which are obtained with the EPE merit function, are similar to the quadrupole illumination mode. Meanwhile, for verifying the superior global convergence performance of the proposed method, the gradient descend (GD) algorithm was executed to accomplish SO. Fig. 12 shows that the simulation results *via* PE and EPE merit functions. From left to right, the simulation results with Patterns 1 to 4 respectively are shown. The first two rows and last two rows represent the simulation results obtained the PE and EPE merit functions, respectively. The intensity distributions of optimized sources with different patterns are approximately the quadrupole illumination.

During these simulations, 150 iterations were executed. Under different conditions, these simulations with GA, PSO, and PSO–GA were all executed five times to assess the convergence efficiency. And the average execution time of these simulations are listed in Table III. The simulations using GD only were run once because there is no randomness in this method. Their running time is shorter than the previous methods. For the different

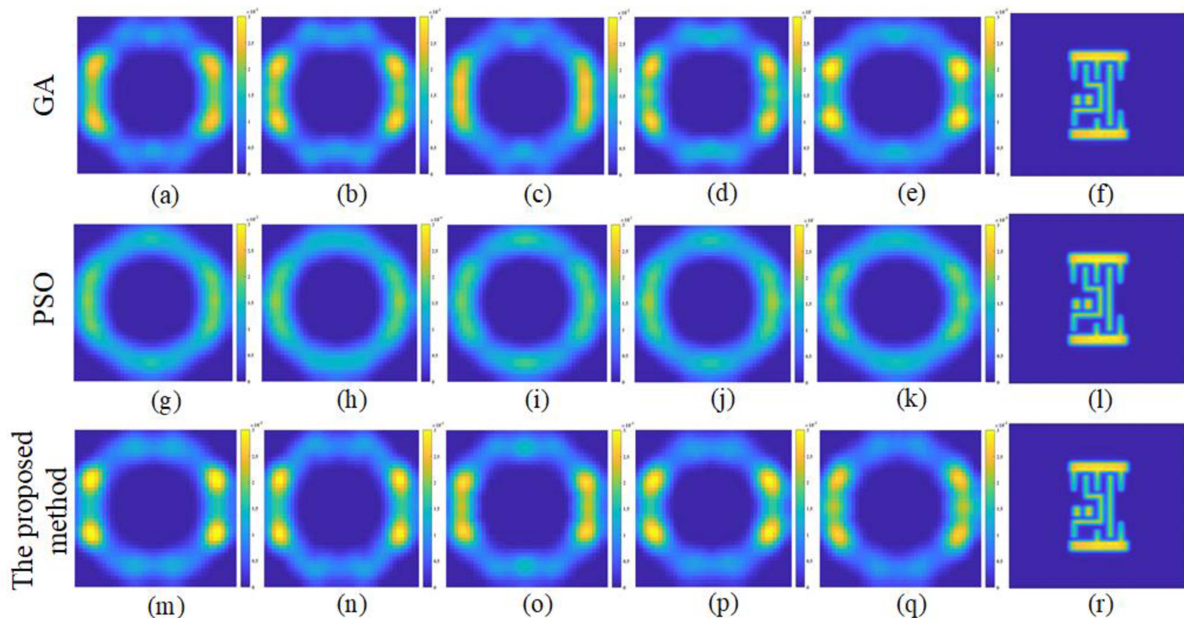

Fig. 11. Simulation results obtained with the EPE merit function for the logical-circuit pattern. From the first row to the third row, the simulation results obtained using GA, PSO, and PSO–GA, respectively, are shown. The first five columns are the optimized sources, and the last column is the intensity distribution of the aerial image.

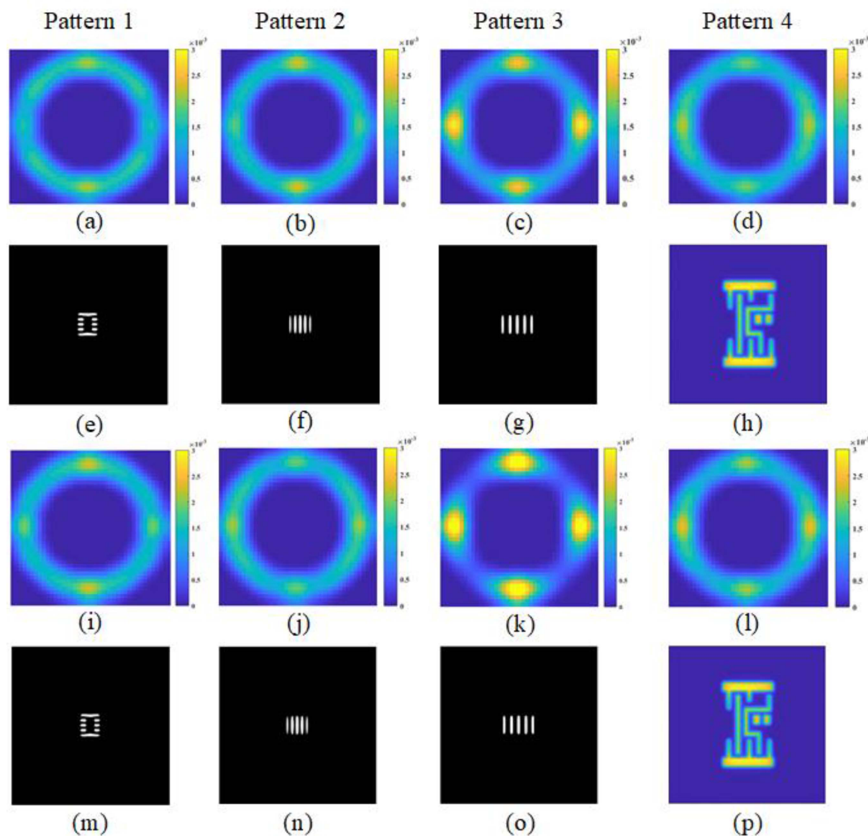

Fig. 12. Simulation results using GD algorithm for different patterns. In the first three columns, the optimized source and resist patterns are shown. From left to right: The simulation results with Pattern 1, Pattern 2, Pattern 3, respectively. The last column shows the optimized source and aerial image with Pattern 4. Rows 1 and 2: The simulation results *via* PE merit function. Rows 3 and 4: The simulation results *via* EPE merit function.

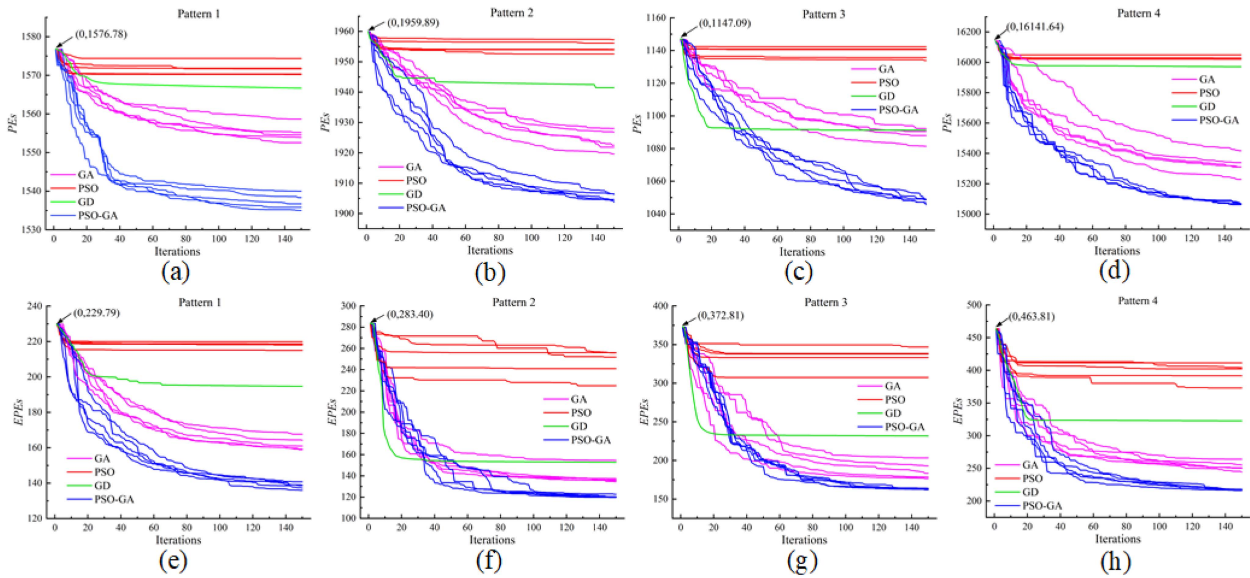

Fig. 13. Convergence curves in the iterative process. Row 1: Convergence curve of the PE merit function as the optimization objective. Row 2: Convergence curve of the EPE merit function as the optimization objective. From left to right: Convergence results of the iteration process using the four different mask patterns. The pink, red, green, and blue curves represent the iterative results obtained using GA, PSO, GD, and PSO–GA, respectively.

patterns, the runtime of simulations via the PE merit function are 248.57, 231.76, 318.59, and 254.31, respectively. And for these simulations via the EPE merit function, the running time are respectively 286.21, 275.82, 304.38, and 217.29. The initial intensity distribution of the pixelated source was initialized to be the same matrix in the simulation process with the same input mask pattern and merit function. The convergence results are illustrated in Fig. 13. The convergence curves obtained with the merit functions, PEs and EPEs, are shown in Fig. 13(a)–(d) and (e)–(h), respectively. In Columns 1–4, the iterative results using different input mask patterns are shown, corresponding to Patterns 1–4, respectively. In all convergence curves, the PSO and GA algorithms stop the search from falling into the local optimum after iteration 20. This is because excess optimization variables complicate the optimization model, hampering the search speed of the method and causing the iteration process to stop prematurely. Conversely, for these SO results obtained by GA, the performance when searching for the global optimum is better than that using PSO. Around iteration 60, the convergence curves show a tendency to retain stability. Owing to the good generalization capability of GA, the optimization performance for the complex variate matrix can be significantly improved by combining PSO with GA in the SO model. The overall search scope can be clearly expanded near the local optimal value, which brings the variate matrix closer to the global optimum. It is, thus, confirmed that the optimization ability applied in the SO model can be enhanced by combining PSO and GA.

IV. Conclusion

In this paper, a hybrid PSO–GA algorithm was proposed to inversely obtain the optimal intensity distribution of the pixelated source in the lithographic-imaging process. To reduce the dispersion degree of the source, Gaussian filtering was implemented to render the pixelated source grayscale. In the proposed SO model, a special imaging model, which is based on the effective spectrum of the mask pattern, was employed for the PCI process. Considering the limitations of PSO and GA in the optimization of the complex variate matrix, they were combined to enhance the convergence performance in the global optimization process. To verify the improvement in the optimization performance, two merit functions: PEs and EPEs, were employed as the optimization objectives. Meanwhile, four mask patterns (including a horizontal block pattern, two different vertical array patterns, and a logical-circuit pattern) were employed as inputs for the optimization model. Upon comparing the simulation results, the global-search scope of the proposed method was found to be significantly improved around the local optimum, bringing it closer to the global optimum. The simulation results demonstrate the superior performance of the proposed SO method for inversely optimizing the intensity distribution of the lithographic-imaging source. Moreover, the proposed hybrid algorithm exhibits a higher convergence capacity than the other traditional algorithms individually.

Acknowledgment

The authors wish to thank the anonymous reviewers for their valuable suggestions.

References

[1] A. K. Wong, *Resolution Enhancement Techniques in Optical Lithography*, vol. 47. Bellingham, WA, USA: SPIE, 2001, doi: 10.1117/3.401208.

[2] D. O. S. Melville et al., “Computational lithography: Exhausting the resolution limits of 193-nm projection lithography systems,” *J. Vac. Sci. Technol. B Nanotechnol. Micro-Electron. Mater. Process. Meas. Phenomena*, vol. 29, no. 6, Nov. 2011, Art. no. 06FH04, doi: 10.1116/1.3662090.

[3] D. S. Abrams and L. Pang, “Fast inverse lithography technology,” *Proc. SPIE*, vol. 6154, 2006, Art. no. 61541J, doi: 10.1117/12.658876.

[4] X. Ma and G. R. Arce, *Computational Lithography*. Hoboken, NJ, USA: Wiley, 2011.

[5] L. Pang, Y. Liu, D. Abrams, and C. Street, "Inverse lithography technology (ILT), what is the impact to photomask industry?," presented at the Photomask and Next Generation Lithography Mask Technology XIII, Yokohama, Japan, May 2006, Art. no. 62830X, doi: 10.1117/12.681857.

[6] J.-C. Yu and P. Yu, "Impacts of cost functions on inverse lithography patterning," *Opt. Exp.*, vol. 18, no. 22, pp. 23331–23342, Oct. 2010, doi: 10.1364/OE.18.023331.

[7] B. Lin et al., "Inverse lithography technology at chip scale," *Proc. SPIE*, vol. 6154, 2006, Art. no. 615414, doi: 10.1117/12.656827.

[8] W. Lv, S. Liu, X. Wu, and E. Y. Lam, "Illumination source optimization in optical lithography via derivative-free optimization," *J. Opt. Soc. Amer. A*, vol. 31, no. 12, pp. B19–B26, Dec. 2014, doi: 10.1364/JOSAA.31.000B19.

[9] X. Ma, Z. Wang, H. Lin, Y. Li, G. R. Arce, and L. Zhang, "Optimization of lithography source illumination arrays using diffraction subspaces," *Opt. Exp.*, vol. 26, no. 4, pp. 3738–3755, Feb. 2018, Art. no. 3738, doi: 10.1364/OE.26.003738.

[10] T. Huang et al., "Improvement of lithography process by using a FlexRay illuminator for memory applications," *Proc. SPIE*, vol. 7973, 2011, Art. no. 79731X, doi: 10.1117/12.879567.

[11] S. Hsu et al., "An innovative source-mask co-optimization (SMO) method for extending low k1 imaging," *Proc. SPIE*, vol. 7140, 2008, Art. no. 714010, doi: 10.1117/12.806657.

[12] K. Iwase et al., "A new source optimization approach for 2X node logic," *Proc. SPIE*, vol. 8166, 2011, Art. no. 81662A, doi: 10.1117/12.898749.

[13] D. DeMaris et al., "Fast source independent estimation of lithographic difficulty supporting large scale source optimization," *Proc. SPIE*, vol. 8326, 2012, Art. no. 832614, doi: 10.1117/12.916433.

[14] A. E. Rosenbluth and N. Seong, "Global optimization of the illumination distribution to maximize integrated process window," *Proc. SPIE*, vol. 6154, 2006, Art. no. 61540H, doi: 10.1117/12.656950.

[15] T. Mülders et al., "Simultaneous source-mask optimization: A numerical combining method," *Proc. SPIE*, vol. 7823, 2010, Art. no. 78233X, doi: 10.1117/12.865965.

[16] O. El-Sewefy et al., "Source mask optimization using 3D mask and compact resist models," *Proc. SPIE*, vol. 9780, 2016, Art. no. 978019, doi: 10.1117/12.2220011.

[17] X. Ma, L. Dong, C. Han, J. Gao, Y. Li, and G. R. Arce, "Gradient-based joint source polarization mask optimization for optical lithography," *Proc. SPIE*, vol. 14, 2015, Art. no. 023504, doi: 10.1117/1.JMM.14.2.023504.

[18] Yao Peng, Jinyu Zhang, Yan Wang, and Zhiping Yu, "High performance source optimization using a gradient-based method in optical lithography," in *Proc. IEEE 11th Int. Symp. Qual. Electron. Des.*, 2010, pp. 108–113, doi: 10.1109/ISQED.2010.5450390.

[19] J.-C. Yu, P. Yu, and H.-Y. Chao, "Fast source optimization involving quadratic line-contour objectives for the resist image," *Opt. Exp.*, vol. 20, no. 7, pp. 8161–8174, Mar. 2012, doi: 10.1364/OE.20.008161.

[20] L. Wang, S. Li, X. Wang, G. Yan, and C. Yang, "Source optimization using particle swarm optimization algorithm in photolithography," *Proc. SPIE*, vol. 9426, 2015, Art. no. 94261L, doi: 10.1117/12.2181335.

[21] J.-C. Yu and P. Yu, "Choosing objective functions for inverse lithography patterning," *Proc. SPIE*, vol. 7973, 2011, Art. no. 79731N, doi: 10.1117/12.879440.

[22] R. Matsui, T. Noda, H. Aoyama, N. Kita, T. Matsuyama, and D. Flagello, "Global source optimization for MEEF and OPE," *Proc. SPIE*, vol. 8683, Apr. 2013, Art. no. 86830O, doi: 10.1117/12.2008267.

[23] X. Ma, D. Shi, Z. Wang, Y. Li, and G. R. Arce, "Lithographic source optimization based on adaptive projection compressive sensing," *Opt. Exp.*, vol. 25, no. 6, pp. 7131–7149, 2017, doi: 10.1364/OE.25.007131.

[24] J. Lin, L. Dong, T. Fan, X. Ma, Y. Wei, and T. Ye, "Learning-based compressive sensing method for EUV lithographic source optimization," *Opt. Exp.*, vol. 27, no. 16, pp. 22563–22581, Aug. 2019, doi: 10.1364/OE.27.022563.

[25] M. Ding et al., "Gradient-based source mask and polarization optimization with the hybrid Hopkins–Abbe model," *Proc. SPIE*, vol. 19, 2020, Art. no. 033201, doi: 10.1117/1.JMM.19.3.033201.

[26] L. Hong, J. Fan, A. Tritchkov, J. Word, and D. Zhang, "Inverse lithography recipe optimization using genetic algorithm," *Proc. SPIE*, vol. 10587, pp. 124–139, 2018, doi: 10.1117/12.2297141.

[27] C. Yang, X. Wang, S. Li, and A. Erdmann, "Source mask optimization using real-coded genetic algorithms," *Proc. SPIE*, vol. 8683, Apr. 2013, Art. no. 86831T, doi: 10.1117/12.2010137.

[28] L. Wang, S. Li, X. Wang, G. Yan, and C. Yang, "Pixelated source optimization for optical lithography via particle swarm optimization," *Proc. SPIE*, vol. 15, 2016, Art. no. 013506, doi: 10.1117/1.JMM.15.1.013506.

[29] H.-F. Kuo and W.-C. Wu, "Forming freeform source shapes by utilizing particle swarm optimization to enhance resolution in extreme UV nanolithography," *IEEE Trans. Nanotechnol.*, vol. 14, no. 2, pp. 322–329, Mar. 2015, doi: 10.1109/TNANO.2015.2393916.

[30] Z. Zhang, S. Li, X. Wang, and W. Cheng, "Fast heuristic-based source mask optimization for EUV lithography using dual edge evolution and partial sampling," *Opt. Exp.*, vol. 29, no. 14, pp. 22778–22795, Jul. 2021, doi: 10.1364/OE.432010.

[31] G. Chen, S. Li, and X. Wang, "Source mask optimization using the covariance matrix adaptation evolution strategy," *Opt. Exp.*, vol. 28, no. 22, pp. 33371–33389, Oct. 2020, doi: 10.1364/OE.410032.

[32] K. Tian et al., "Benefits and trade-offs of global source optimization in optical lithography," *Proc. SPIE*, vol. 7274, Mar. 2009, Art. no. 72740C, doi: 10.1117/12.814305.

[33] C. Yang, S. Li, and X. Wang, "Efficient source mask optimization using multipole source representation," *Proc. SPIE*, vol. 13, 2014, Art. no. 043001, doi: 10.1117/1.JMM.13.4.043001.

[34] T. Fühner, A. Erdmann, R. Farkas, B. Tollkühn, and G. Kókai, "Genetic algorithms to improve mask and illumination geometries in lithographic imaging systems," in *Applications of Evolutionary Computing*, vol. 3005, G. R. Raidl, et al. Ed. Berlin, Germany: Springer, 2004, pp. 208–218, doi: 10.1007/978-3-540-24653-4_22.

[35] Y. Sun et al., "Sampling-based imaging model for fast source and mask optimization in immersion lithography," *Appl. Opt.*, vol. 61, no. 2, pp. 523–531, Jan. 2022, doi: 10.1364/AO.437655.

[36] Z. Song, X. Ma, J. Gao, J. Wang, Y. Li, and G. R. Arce, "Inverse lithography source optimization via compressive sensing," *Opt. Exp.*, vol. 22, no. 12, pp. 14180–14198, Jun. 2014, doi: 10.1364/OE.22.014180.

[37] Y. Sun, Y. Li, T. Li, X. Yan, E. Li, and P. Wei, "Fast lithographic source optimization method of certain contour sampling-Bayesian compressive sensing for high fidelity patterning," *Opt. Exp.*, vol. 27, no. 22, pp. 32733–32745, Oct. 2019, doi: 10.1364/OE.27.032733.

[38] Z. Drezner and A. Misevičius, "Enhancing the performance of hybrid genetic algorithms by differential improvement," *Comput. Operations Res.*, vol. 40, no. 4, pp. 1038–1046, Apr. 2013, doi: 10.1016/j.cor.2012.10.014.

[39] Q. Yuan and F. Qian, "A hybrid genetic algorithm for twice continuously differentiable NLP problems," *Comput. Chem. Eng.*, vol. 34, no. 1, pp. 36–41, Jan. 2010, doi: 10.1016/j.compchemeng.2009.09.006.

[40] P. Dziwinski and L. Bartczuk, "A new hybrid particle swarm optimization and genetic algorithm method controlled by fuzzy logic," *IEEE Trans. Fuzzy Syst.*, vol. 28, no. 6, pp. 1140–1154, Jun. 2020.

[41] M. M. Noel and T. C. Jannett, "Simulation of a new hybrid particle swarm optimization algorithm," in *Proc. 36th Southeastern Symp. Syst. Theory*, Atlanta, GA, USA, 2004, pp. 150–153. doi: 10.1109/SSST.2004.1295638.

[42] Y. Cao, H. Zhang, W. Li, M. Zhou, Y. Zhang, and W. A. Chaovalitwongse, "Comprehensive learning particle swarm optimization algorithm with local search for multimodal functions," *IEEE Trans. Evol. Comput.*, vol. 23, no. 4, pp. 718–731, Aug. 2019, doi: 10.1109/TEVC.2018.2885075.

[43] G. Tian, Y. Ren, and M. Zhou, "Dual-objective scheduling of rescue vehicles to distinguish forest fires via differential evolution and particle swarm optimization combined algorithm," *IEEE Trans. Intell. Transp. Syst.*, vol. 17, no. 11, pp. 3009–3021, Nov. 2016.

[44] A. K.-K. Wong, *Optical Imaging in Projection Microlithography*. Bellingham, WA, USA: SPIE, 2005.

[45] P. Evanschitzky, A. Erdmann, and T. Fühner, "Extended Abbe approach for fast and accurate lithography imaging simulations," in *Proc. 25th Eur. Mask Lithography Conf.*, 2009, Art. no. 747007, doi: 10.1117/12.835168.

[46] R. Koehle, "Fast TCC algorithm for the model building of high NA lithography simulation," *Proc. SPIE*, vol. 5754, pp. 918–929, 2005, doi: 10.1117/12.599591.

[47] J. Shang, Y. Tian, Y. Liu, and R. Liu, "Production scheduling optimization method based on hybrid particle swarm optimization algorithm," *J. Intell. Fuzzy Syst.*, vol. 34, no. 2, pp. 955–964, Feb. 2018, doi: 10.3233/JIFS-169389.

[48] H. Zhu, Y. Hu, and W. Zhu, "A dynamic adaptive particle swarm optimization and genetic algorithm for different constrained engineering design optimization problems," *Adv. Mech. Eng.*, vol. 11, no. 3, Mar. 2019, Art. no. 168781401882493, doi: 10.1177/1687814018824930.

[49] D. Whitley, "A genetic algorithm tutorial," *Statist. Comput.*, vol. 4, pp. 65–85, Jun. 1994, doi: 10.1007/BF00175354.

[50] L. Haldurai, T. Madhubala, and R. Rajalakshmi, "A study on genetic algorithm and its applications," *Int. J. Comput. Sci. Eng.*, vol. 4, no. 10, pp. 139–143, 2016.